Detection of Rotation in a Binary Microlens: PLANET Photometry of MACHO 97-BLG-41

M. D. Albrow[1], J.-P. Beaulieu[2,3], J. A. R. Caldwell[4], M. Dominik[2], B. S. Gaudi[5], A. Gould[5], J. Greenhill[6], K. Hill[6], S. Kane[6,7], R. Martin[9], J. Menzies[4], R. M. Naber[2], K. R. Pollard[1], P. D. Sackett[2,8], K. C. Sahu[7], P. Vermaak[4], R. Watson[6], A. Williams[9]

(The PLANET Collaboration)
and
H.E. Bond[7], I.M. van Bemmel[10,2]

ABSTRACT

We analyze PLANET collaboration data for MACHO 97-BLG-41, the only microlensing event observed to date in which the source transits two disjoint caustics. The PLANET data, consisting of 46 V-band and 325 I-band observations from five southern observatories, span a period from the initial alert until the end of the event. Our data are incompatible with a static binary lens, but are well fit by a rotating binary lens of mass ratio $q = 0.34$ and angular separation $d \approx 0.5$ (in units of the Einstein ring radius) in which the binary separation changes in size by $\delta d = -0.070 \pm 0.009$ and in orientation by $\delta\theta = 5°.61 \pm 0°.36$ during the 35.17 days between the separate caustic transits. We use this measurement combined with other observational constraints to

derive the first kinematic estimate of the mass, distance, and period of a binary microlens. The relative probability distributions for these parameters peak at a total lens mass $M \sim 0.3\,M_\odot$ (M-dwarf binary system), lens distance $D_{\rm L} \sim 5.5\,{\rm kpc}$, and binary period $P \sim 1.5\,{\rm yr}$. The robustness of our model is demonstrated by its striking agreement with MACHO/GMAN data that cover several sharp features in the light curve not probed by the PLANET observations, and which did not enter our modeling procedure in any way. Available data sets thus indicate that the light curve of MACHO 97-BLG-41 can be modeled as a source crossing two caustics of a physically-realistic rotating binary so that, contrary to a recent suggestion, the additional effects of a postulated planetary companion to the binary lens are not required.

Subject headings: binaries: general — gravitational lensing — planetary systems

1. Introduction

One of the first microlensing events discovered was shown to be due to a binary lens (Udalski et al. 1994), not surprisingly since most of the hundreds of events discovered toward the Galactic bulge are believed to be due to normal stellar lenses in the disk and bulge of the Milky Way (cf., Kiraga & Paczyński 1994; Zhao, Spergel & Rich 1995; Alcock et al. 1997) and a sizable fraction of stars reside in binary systems. However, not all binary lenses can be recognized readily as such. For typical photometric sampling and precision, most light curves generated by double lenses will be indistinguishable from single-lens events if one lens component is sufficiently less massive than the other or if the components are separated by angular distances sufficiently smaller or larger than the Einstein ring radius. Nevertheless, several binary microlens events are recognized every year (cf. Alcock et al. 1999), generally through sharp peaks in their light curves that betray the presence of extended caustic structure (closed and sometimes disjoint curves of formally infinite magnification on the sky) which are not generated by single point-lenses.

Binary lenses have already demonstrated their importance to astronomy in several ways. Timing the motion of a caustic across a finite background source of known size can be used to measure the relative proper motion of the lens and source. This was done by several groups who performed a joint analysis (Afonso et al. 2000 and references therein) of their data to demonstrate beyond reasonable doubt that the lensing system of event MACHO 98-SMC-1 was not a constituent of Galactic dark matter, but a normal stellar binary in the Small Magellanic Cloud (SMC) itself. Caustic structure differentially magnifies background sources, providing a means of measuring limb-darkening coefficients for their stellar atmospheres, as has been done for a K-giant in the Galactic bulge (Albrow et al. 1999a) and an A-dwarf in the SMC (Afonso et al. 2000). Mathematically, lensing planetary systems represent the extreme-mass-ratio subset of binary (or multiple) lenses (Mao & Paczyński 1991; Dominik 1999). Two groups (PLANET, Albrow et al. 1998; MPS, Rhie et al. 1999a) are conducting intense monitoring projects specifically designed to search for lensing planets. The efficiency with which planets can be detected must be determined separately for each light curve (Gaudi & Sackett 2000); massive planetary companions have been ruled out over a wide range of separations for two different microlenses (Rhie et al. 1999b; Albrow et al. 1999c).

The components of all physical binaries rotate about their common center of mass, a phenomenon that alters the shape and relative placement of caustic curves on the sky and thus, in principle, the form of any light curve generated by a binary microlens (Dominik 1998). Nevertheless, rotation has not yet been demonstrated in any binary microlens.

The unusual light curve of the Galactic bulge microlensing event MACHO 97-BLG-41

displays what appear to be source crossings of two disjoint caustic curves separated in time by about a month. The event has already been discussed by two groups with extensive photometric data sets: MACHO/GMAN, who report that they were unable to find a static or rotating binary model compatible with their data (Alcock et al. 1999), and MPS/Wise-GMAN (Bennett et al. 1999), who — based on MPS+MACHO/GMAN data — also discount rotation as an explanation for the features in the light curve, concluding that a three-body lens (binary + orbiting Jovian planet) is required to produce the light curve structure in MACHO 97-BLG-41. Theirs is the first claim in the literature for a planet orbiting a normal binary stellar system, as opposed to one component of a binary (Butler et al. 1997; Cochran et al. 1997) or a binary pulsar (Thorsett et al. 1999). Given the small chances of discovering such a system from microlensing observations, Bennett et al. (1999) argued that they might well be common.

Here, we present and analyze the PLANET photometric data set for MACHO 97-BLG-41, which is completely independent of the MPS+MACHO/GMAN data set analyzed by Bennett et al. (1999). We also find that no static binary model reproduces our data, but unlike Bennett et al. (1999) we conclude that a rotating binary model, with physically realistic parameters, does provide a satisfactory fit to all features in our light curve. Since the two data sets are disjoint (and since the MACHO/GMAN data sample key caustic-crossing regions that our data do not) we examine whether or not our solution can provide a satisfactory fit to their data. We find that our solution (derived without reference to any data but our own) is in reasonable agreement with MACHO/GMAN data, so that it appears likely that a single rotating-binary solution near the one we have found is consistent with all available data. This result obviates the need for a third lensing component (planet) to explain the unusual light curve of MACHO 97-BLG-41.

We describe our data for MACHO 97-BLG-41 and their reduction in §2. Our general form for a rotating binary model is given in §3. Our modeling analysis is presented in §4, including a demonstration of the non-viability of static binary models, and of the success of the rotating binary model in fitting not only our data but also the MACHO/GMAN data set for MACHO 97-BLG-41 used in Bennett et al. (1999). In §5 we present the physical and kinematical parameters for the binary lens derived from our analysis of our data, including the first statistical estimate for the mass and rotational period of a lensing binary made possible by our measurement of rotation in this system. We conclude in §6 that MACHO 97-BLG-41 is the first microlensing event in which binary lens rotation has been demonstrated, and that it provides a credible, physically-realistic, and elegant model for this complex light curve.

2. PLANET Photometric Data for MACHO-97-BLG-041

An electronic alert of the microlensing event MACHO 97-BLG-41 was issued on 18 June 1997 by the MACHO[11] team. Many such alerts are made each year by the MACHO, OGLE[12] and EROS[13] collaborations, allowing a variety of follow-up observations to be undertaken by other teams. The MACHO 97-BLG-41 event was described in the MACHO alert as in the direction of the Galactic bulge ($\alpha =$17:56:20.7, $\delta = -$28:47:42) and possibly of short duration. The PLANET collaboration began monitoring immediately. On 29 June 1997, MACHO reported that the light curve of the event had flattened, but at a level above its baseline value, in a manner consistent with expectations for a binary lens. On 2 July 1997, PLANET[14] reported an increase of brightness of a few percent, and on 23 July 1997 predicted that a caustic crossing was likely to occur the following day at JD - 2450000 $=$ 654 ± 1; this was subsequently confirmed observationally by both MACHO and PLANET.

The PLANET data set for MACHO 97-BLG-41 consists of photometric measurements in the V band from three observing sites and in the I band from five observing sites in the Southern Hemisphere during a four-month period directly after the initial alert. In addition, six measurements were taken after the event had reached baseline in April 1998 at the Canopus 1.0m in Tasmania with the same detector system as used in 1997. The data set thus comprises 8 separate light curves.

After flat-fielding and bias subtraction, the source star was photometered using the image subtraction package ISIS 2.0 (Alard 1999). In this procedure, pixel values are first interpolated to register all frames to an image chosen as the astrometric reference for that band and site. A photometric template is then formed for each band and site from several good-seeing, low-background frames. ISIS 2.0 uses a non-constant kernel with a fixed number of variable parameters to transform the template to each image by performing a least squares fit to derive the values of the kernel parameters. Profile-fitting photometry is then performed to measure the flux difference of variable objects between each frame and the template by convolving the point spread function (PSF) of the template with the best-fitting PSF matching kernel for each of the images. Frame-to-frame differences in exposure time, background, transparency, and the size and shape of the point spread function are automatically taken into account with this package, but since only flux

---

[11]MACHO/GMAN Alert Homepage: http://darkstar.astro.washington.edu

[12]OGLE Alert Homepage: http://www.astrouw.edu.pl/~ogle/ogle2/ews/ews.html

[13]EROS Alert Homepage: http://www-dapnia.cea.fr/Spp/Experiences/EROS/alertes.html

[14]PLANET Collaboration Homepage: http://www.astro.rug.nl/~planet

differences are measured, the photometric system must be aligned with a standard system. We have done this by performing a linear regression between ISIS flux differences and DoPHOT-reported fluxes (see below), and placing the latter on a standard system using standard stars. The ISIS 2.0 package produces a quality parameter to indicate the quality of the subtraction, which is a function of the signal-to-noise in the subtracted frame. To produce the cleaned data set used for analysis, we require that this quality flag is greater than 0.9, eliminating the poorest $\sim$35% of the frames. In addition, we have discarded 9 other frames for insufficient exposure time, very strong disagreement with data taken at nearly the same time on a smoothly varying portion of the light curve, or sensitivity to V-band limb-darkening (3 V-band points too near a caustic), which we cannot constrain. The result is 325 I-band and 46 V-band measurements, for a grand total of 371 points in the high-quality, cleaned ISIS data set. A summary is given in Table 1.

We have also reduced our data set with the PSF-profile-fitting package DoPHOT (Schechter, Mateo, & Saha 1993), using fixed-position catalogs and the average of four or more stable, moderately bright and relatively uncrowded stars in the field as a relative flux standard (Albrow et al. 1998). Final cleaned DoPHOT-reduced data sets were formed by eliminating all trailed frames, frames that did not process properly, or frames whose image quality or signal-to-noise were not adequate to produce reliable (i.e., DoPHOT type 11) measurements for the source star or the relative flux standard. Instrumental magnitudes of the SAAO 1m DoPHOT system were then calibrated against contemporaneous observations of Johnson-Cousins, UBV(RI)c E-region standards (Menzies et al. 1989) at the beginning of the 1999 observing season. The instrumental magnitudes of other PLANET sites were brought to this system in the modeling process by introduction of an alignment parameter for every site and band. This parameter is insensitive to widely different models and thus has no effect on the results we present here. Linear regression between the ISIS flux differences and the calibrated DoPHOT fluxes then allowed calibration of the ISIS dataset.

The eight ISIS-reduced light curves of MACHO 97-BLG-41 are shown in Figure 1, in which we have overplotted the best-fitting model presented in §4.3 used to photometrically align the multi-site data. Due to differences in effective resolution at different sites and in different bands, each light curve can be subject to different amounts of non-lensed blended light. The model yields a best fit to this blended light so that we can plot the magnification of the lensed source light only in Figure 1. Plotting magnifications in Figure 1 also allows presentation of V- and I-band data on the same plot, since the unlensed source magnification is by definition equal to unity irrespective of passband.[15] The time scale has

---

[15] Technically, the V- and I-band magnification curves can differ in regions such as caustic crossings where the passband-dependent source profile is important. Since we have eliminated the few V-band points in these

been expressed in Heliocentric Julian Date (HJD) at the middle of the exposure, with a fixed offset: $\mathrm{HJD}' = \mathrm{HJD} - 2450000$. We use this timing system throughout.

2.1.   Reddening of the MACHO 97-BLG-41 Field from the CMD

Figure 2 displays a color-magnitude diagram (CMD) of a $1' \times 1'$ field centered on MACHO 97-BLG-41 derived from SAAO 1m images. The position of the unmagnified source star is shown together with that of the blend (unresolved light along the line of sight), as determined from the models presented in §4.2. Comparison of this CMD with one for a larger $5' \times 5'$ field clearly indicates that the reddening is variable across the field.

Using our standard-star calibration of this $1'$ subfield, we find that the center of the red clump is at $I_{\mathrm{cl}} = 16.20 \pm 0.05$ and $(V - I)_{\mathrm{cl}} = 2.55 \pm 0.05$. Comparing this observed color to the dereddened color of $(V - I)_{\mathrm{cl},0} = 1.114$ derived by Paczyński et al. (1999), we obtain a value of the reddening $E(V - I) = 1.44$. The reddening law $A_I = 1.49 E(V - I)$ of Stanek (1996) then yields $A_I = 2.15$. In §5 we will use this value of reddening and extinction together with our best estimate of the color and magnitude of the source from our modeling to derive an angular size for the source and thence the relative lens-source proper motion.

3.   Model Parameters for a Rotating Binary Microlensing Event

A static, binary lensing event of an unblended finite source can be described by the seven parameters: d, the angular separation between the two masses as a fraction of the angular Einstein radius θ_{E}; $q \equiv M_2/M_1$, the mass ratio of the two components; the Einstein time $t_{\mathrm{E}} \equiv \theta_{\mathrm{E}}/\mu$, where μ is the relative proper motion between the source and the binary center of mass; t_0, the time of closest angular approach between the source trajectory and the binary center of mass; u_0, the angular separation between the source and binary center of mass at time t_0 in units of θ_{E}; α, the angle of the source trajectory on the sky relative to the binary axis; and ρ_*, the angular size of the source star in units of θ_{E}.

Throughout, we use the Einstein ring radius of the total mass M,

$$\theta_{\mathrm{E}}^2 \equiv \frac{4GMD_{\mathrm{LS}}}{c^2 D_{\mathrm{L}} D_{\mathrm{S}}} \quad , \tag{1}$$

---

regions, this is not a concern for us here.

where $D_{\rm L}$ is the observer-lens distance, $D_{\rm S}$ is the observer-source distance, and $D_{\rm LS} \equiv D_{\rm S} - D_{\rm L}$. We center our coordinate system on the center of mass of the binary lens such that at time t_0 the lenses are aligned with the x-axis, with the more massive of the two, M_1 on the right. The angle α is chosen between the positive x-axis and the source trajectory so that M_1 remains to the right of the source.

A binary system in which each partner travels on an ellipse about the common center of mass is described by the seven parameters of the reduced Kepler problem: the semi-major axis a, the period P, the eccentricity e, the phase ϕ (at time t_0, say), and the three angles of orientation. However, two of these, a and one of the orientation angles, are already contained in the parameterization of a static lens microlensing event (in which distances are expressed in $\theta_{\rm E}$ and positions measured relative to the source trajectory), leaving five *additional* parameters specific to binary rotation. If the motion is circular ($e = 0$), three of these canonical parameters remain: P, ϕ, and the inclination of the orbital plane with respect to the sky.

We model our MACHO 97-BLG-41 data with the simplest rotation model required to fit all the observed features, namely rectilinear relative motion of the lens components, which represents the next higher order term in lens motion compared to a static binary lens. Only the two components of this motion that lie in the sky plane are measurable since motion along the line-of-sight does not alter the caustic structure of the binary. We could expect to be able to detect the relative acceleration of the binary components only if we have a very strong detection of the rectilinear motion and the observations cover a sizable fraction of the rotation period. We therefore model the binary rotation by adding only two degrees of freedom over that required for the static binary: Δ_x and Δ_y, which measure the evolution of the separation vector during the course of the observations in the x- and y-directions. Under our assumption of rectilinear motion, the separation vector is thus

$$\vec{d} = \vec{d_0} + \vec{\Delta} \left(\frac{t - t_0}{t_{\rm E}} \right) \tag{2}$$

where $\vec{d_0} \equiv (d_0, 0)$ is the separation vector at time t_0, and $\vec{\Delta} \equiv (\Delta_x, \Delta_y)$. This formulation has the advantage that we need not assume anything about the eccentricity of the orbit. The assumption of circular orbits would reduce the complexity of the full orbital solution, but is unlikely to be valid for the stellar binaries separated by several AU to which microlensing is sensitive (Duquennoy & Mayor 1991). Regardless of the eccentricity of the orbit, the first order term we are attempting to measure is the sky velocity of the separation vector. As we explain in §4.2, however, it is both inconvenient and time-consuming to parameterize the search for rotating solutions in terms of the 9 (7 static + 2 rotating) canonical parameters.

We will search for solutions using a different set of parameters, translating our final models back to the canonical system at the end of the process.

In addition to these parameters, for each of the $n = 8$ light curves, model parameters must be assigned for the flux of the source star, F_S and the unlensed background flux, F_B. These can vary among sites due to differences in calibration of instrumental magnitudes and effective spatial resolution. We also include a parameter η_{see} for each light curve to fit a linear relation to the systematic trends between measured flux and seeing generally seen in our data (cf. Albrow et al. 1999c). The flux of light curve i is thus modeled as

$$F_i(t) = F_{S,i}\, A(t) + F_{B,i} + \eta_{see,i}\, [\theta_{FWHM,i}(t) - 2''] \,, \tag{3}$$

where $\theta_{FWHM,i}$ is the FWHM of the seeing disk, and A is the magnification from the model.

Finally, since caustic structure can differentially magnify the finite source, we include a limb-darkening parameter Γ_I. Our limb-darkening parameter Γ is related to the canonical linear limb-darkening coefficient c through $c_I = 3\Gamma_I/(\Gamma_I + 2)$ (Albrow et al. 1999b, Appendix B). Because our V data are not sufficient to constrain Γ_V, we eliminate this parameter from our modeling and the 3 V-band points that could be affected by it.

In sum, we require 9 physical parameters for the rotating binary, $3n = 24$ for the multi-site photometric alignment, blending, and systematic seeing correlations, and 1 for source I-band limb darkening, for a grand total of 34 model parameters. We describe how we search for solutions in this unwieldy parameter space in §4.2.

4. Light Curve Analysis

The PLANET light curve of MACHO 97-BLG-41 in Figure 1 shows two temporally sharp features, one at HJD$'$ =619 and a second at HJD$'$ =654. Between these two broad features, the magnification is substantially less than $A = 3$, so that unless the source is strongly blended, it cannot be inside a caustic in this region (Witt & Mao 1995).

The leading rise and roll-over at HJD$'$ =650 indicates an approach to one cusp (a sharp discontinuous feature in a caustic curve) before the actual crossing near a second cusp of the same caustic at HJD$'$ =654. This crossing must have begun after HJD$' = 653.21694$, our last point on the gentle leading shoulder of the second peak. The end of the crossing is marked by the ultra-steep decline in brightness near HJD$'$ =654.5. In the interval $654.50156 \leq$HJD$' \leq 654.53788$, the magnification is falling quite rapidly at a linear rate of $\mathrm{d}A/\mathrm{d}t = -133.7 \pm 1.6\,\mathrm{day}^{-1}$.

The first anomaly, which ends near $HJD' \sim 619$, initially triggered the microlensing alert of MACHO 97-BLG-41, then thought to be a normal short duration single-lens event. The points in the interval $619.33864 \leq HJD' \leq 619.65447$ fall smoothly with a slope of $dA/dt \sim -2.3\,\mathrm{day}^{-1}$ which, although rapid, is considerably slower than the rate seen during the caustic crossing near $HJD' = 654.5$. The concavity and moderate steepness of the light curve near HJD'$= 619$ indicates that the source exits a caustic very close to or over a cusp, and approximately parallel to its axis. The crossing must have begun before our first SAAO data point at $HJD' = 619.34$. We note that the concavity of our data in this region is inconsistent with the particular three-body solution presented by Bennett et al. (1999), though these data alone do not preclude the possibility of a different three-body solution.

4.1. Failure of Static Models

The number, shape, and relative orientation of the closed caustic curves generated by a binary lens are fixed by its mass ratio q and separation d, so that information about the caustics from the light curve constrain these two quantities (Schneider & Weiss 1986; Erdl & Schneider 1993; Dominik 1999). For a given q, wide separations produce two diamond (4-cusped) caustics; close separations generate three caustics, one diamond and two triangular (3-cusped); intermediate separations produce one 6-cusped caustic. In all cases, one of the caustics, called the central caustic, will be near the position of the more massive lens.

Because the second peak in the light curve of MACHO 97-BLG-41 sits atop a region of higher background magnification than the first, it is likely to be associated with the central caustic. The cusp approach at $HJD' =650$ *between* two widely separated crossings that are themselves near or over cusps does not support the notion that all three are due to the single caustic produced by an intermediate-separation binary. The proximity of the cusp-approach shoulder at $HJD' =650$ to the near-cusp crossing near $HJD' =654$ constrains the size of the central caustic to be rather small compared to the Einstein radius θ_{E}, an indication that the mass ratio q is not near unity, $d \ll 1$, or $d \gg 1$. In the last category, caustics are symmetric about the line joining them (the binary axis). Since the light curve of MACHO 97-BLG-41 is strongly asymmetric about the second caustic crossing, the source trajectory must be poorly aligned with the binary axis and thus could not cross the other caustic of a wide binary unless the binary were rapidly rotating. On the other hand, the triangular caustics of close binaries with mildly unequal masses are naturally positioned at an angle with respect to the axis of symmetry of the central caustic. We therefore begin by exploring binary models of this type, asking whether the light curve could be produced

by the source traversing the magnification pattern of a close binary whose caustics remain motionless during the course of the event.

Strikingly, and despite the fact that our data do not cover either caustic crossing very well, we find that no static binary provides a good fit to the data. Static models that reproduce the structure of the strongly asymmetric second peak cannot reproduce the first caustic region because the source fails to pass through either of the smaller triangular caustics at an earlier time. (The topology of the central and triangular caustics can be appreciated by examining Fig. 3.) For the same reason, static models that fit the first light curve feature are very poor fits to the second. A static binary microlens model simply cannot explain the features of our data for MACHO 97-BLG-41. Bennett et al. (1999) came to the same conclusion based on their data for this event, which also led them to search for a rotating binary solution. Finding no viable rotating model, they concluded that the first caustic crossing was not due to one of the binary's own "natural" caustics, but to additional caustic structure induced by a planet. We turn now to the viability of a rotating binary model for MACHO 97-BLG-41.

4.2.   Success of Rotating Models

For certain orientations and data samplings, planetary anomalies may be confused with those caused by triangular caustics of close binaries with higher mass ratio. Although the position of the triangular caustic in static models of MACHO 97-BLG-41 is too misaligned with the source trajectory to explain the first caustic peak, its *size* is compatible with the duration of the first peak, in both our data and those used by Bennett et al. (1999). We found that models that simply rotate this caustic pattern on the sky yield many of the essential features of the light curve. Encouraged by this, and recognizing that caustic crossings widely separated in time should offer the best chance for detecting binary rotation, we proceeded to a quantitative search for rotating binary models as described in the following section.

4.2.1.   Search Strategy

As we noted in §3, a rotating binary observed for a small fraction of its period can be approximated as two masses moving in straight lines about their common center of mass. We parameterize this system by beginning with the 7 parameters that characterize a static binary event $(d_0, q, t_E, t_0, u_0, \alpha, \rho_*)$, and add Δ_x and Δ_y to account for the two dimensions

of (projected) relative velocity of the binary. Once a model characterized by these 9 parameters is chosen, the best fit for the additional photometric parameters $F_{S,i}$, $F_{B,i}$ and $\eta_{see,i}$ can be determined by linear fitting, which requires a negligible amount of computer time. Hence, the complexity of the problem is basically determined by the character of the 9-parameter space.

In practice, it is quite difficult to search this canonical parameter space by means of standard χ^2 minimization routines, in part because the dimensionality is large, but mainly because the χ^2 surface is highly irregular. A useful approach is to seek an alternative empirical parameterization of the problem in which some of the parameters are fixed, or at least highly constrained by subsets of the data. For example, Albrow et al. (1999b) showed that for static binaries with a well-sampled fold-caustic crossing, it is possible to reduce the primary search space from 7 to 5 dimensions by choosing the parameterization carefully. Moreover, they were able to restrict the 5-dimensional search to points outside of caustics (for which finite source effects can be ignored or handled analytically so that the magnification can be evaluated 100 or even 1000 times faster than for caustic-crossing points), thereby rendering a 5-dimensional brute-force search tractable.

Here we develop a similar strategy. Three quantities are relatively well determined by cursory inspection of our data: the time the center of the source exits the first caustic $t_{cc,1}$, the time the trailing limb exits the second caustic $t_{ce,2}$, and the minimum separation from the source center relative to the first cusp $u_{c,1}$. We construct a parameterization with these three quantities fixed at initial guesses derived from inspection of the data so that the search can be restricted to the remaining six parameters. More specifically, by linearly extending the light curves from just before and just after the end of the crossing (see e.g. Afonso et al. 1998), we find that the end of the second crossing is at $t_{ce,2} = t_{cc,2} + \Delta t_2 = 654.544 \pm 0.001$ days. Here Δt_2 is the radius crossing time of the source over the second caustic so that $t_{cc,2}$ is the time the source center egresses.

We begin our fitting process by assuming that the center of the source passes exactly over the first cusp at $t_{cc,1} = 619.34$, our first data point in the series of SAAO 1m points on the concave decline. After one iteration, we find that a better estimate is that the center passes closest to the cusp of the first caustic at $t_{cc,1} = 619.15$. The time between caustic crossings is then $\delta t \equiv t_{cc,2} - t_{cc,1} \simeq 35.18$ days, where we have made the evaluation based on our final measurement of Δt_2. The six remaining parameters allowed to vary in our search are $(d_{mid}, q, \ell_2, \Delta t_2, \delta d, \delta\theta)$. Here d_{mid} is the average of the separations d_1 and d_2 at the times of the caustic crossings $t_{cc,1}$ and $t_{cc,2}$, ℓ_2 is the coordinate of the egress point on the central diamond caustic relative to the cusp (as measured along the cusp bisector) in units of θ_E, δd is the change in the binary separation d during δt, and $\delta\theta$ is the change in

binary orientation during δt. In our sign convention, $\delta d > 0$ and $\delta\theta > 0$ imply a binary lens that is separating and rotating counterclockwise on the sky with time.

We initiate our search for rotating solutions by considering only data from $t > 621$ (and encapsulate all the information from the earlier data in the assumption that the source crosses the cusp at $t = t_{cc,1}$). All but 5 of these points are outside the caustics and so require only a single call to the lens solver to evaluate the magnification. Hence, the entire light curve can be evaluated quickly ($\sim$1 second on our system), permitting a very rapid search of the 6 dimensional space. For each such model near a minimum in χ^2, we examine a grid of models for the early data points $t < 621$. This grid is characterized by two parameters, namely the two parameters we had held fixed earlier: the time of the first caustic exit and the position of the source relative to the cusp at this crossing. A full integration over the source is required for most of these early points, but since the search is on a 2-dimensional grid, it can be performed in about 4 minutes. For each 6-dimensional model, we add the additional χ^2 from the best 2-dimensional grid to obtain the overall χ^2.

4.2.2. Results

Joint fits to the multi-site multi-band cleaned ISIS data were performed using the empirical parameters and discrete-grid strategy described in the previous section. The parameters of this minimum were then converted to the canonical parameterization, and the minimum checked via a more conventional, but time-consuming, search using a downhill simplex method beginning with a seed near the empirical solution. Since the formal errors reported by photometric reduction packages often do not represent the true scatter in crowded-field data, systematic effects are often present that depend on site and target star. We therefore multiply the error bars of each of our 8 light curves by scaling factors σ/σ_{ISIS} that force $\chi_i^2/(N_i - 3) = 1$, where N_i is the number of data points in light curve i. (Three degrees-of-freedom are already used by the $F_{S,i}$, $F_{B,i}$ and $\eta_{see,i}$ fitting parameters.) These error bar scaling factors, given in Table 1, are necessary to ensure that light curves with substantially underestimated photometric uncertainties are not given more weight than they are due in the joint fit. As an aside, we note that these scaling factors are closer to unity for ISIS reductions than for DoPHOT reductions in most cases we have tested, apparently indicating that ISIS-reported errors more accurately reflect the true scatter in the photometric data.

Photometric parameters that depend on site, detector, and passband are presented in Table 1 for the resulting best-fitting model to the cleaned ISIS data set. In Table 2 we list the nine empirical geometric fitting parameters and their corresponding canonical

counterparts for both data sets. Uncertainties are presented for the fitted parameters; canonical parameters are expressed to more digits than are significant since this precision is required to reproduce the solution described by the fitted parameter set.

To specify a solution to a multi-parameter problem to better than $\Delta\chi^2 = 1$, one must give each parameter i to a precision $B_{ii}^{-1/2}$, where $B \equiv C^{-1}$ and C_{ij} is the covariance matrix. If the parameters are highly correlated, as they are for the canonical parameters of a rotating binary, then $B_{ii}^{-1/2} \ll C_{ii}^{1/2}$, so that the individual parameters must be specified to much higher precision than the statistical errors. When we convert from the empirical to canonical parameters, we find that numerical errors enter that are small compared to $C_{ii}^{1/2}$ but comparable to $B_{ii}^{-1/2}$. We therefore minimize χ^2 for the canonical parameters using downhill simplex with the transformed solution as our starting point. This refined minimum is given as the last column of Table 2.

Most of the parameters in the two solutions are very similar, but c_I differs by $\sim 0.6\sigma$. Thus our two minimization routines associated with our two parameterizations agree at $\Delta\chi^2 < 1$ but not at $\Delta\chi^2 \ll 1$, indicating that one or both has numerical errors at this level. Since the numerical errors are smaller than the statistical errors, they are of no concern here, but would be if the quality of the data could be improved by a factor ten.

We have computed the full matrix of correlation coefficients for our empirical, geometric fitting parameters and have found that the parameters $Deltat_2$ and Γ_I are anti-correlated at the 94% level. This strong anti-correlation arises because the majority of the constraint on Γ_I comes from the 5 SAAO data points near $\text{HJD}' = 654.5$, for which the limb of the source was exiting the second caustic. Measurements near the end of a caustic crossing are subject to a degeneracy between the source size and limb darkening, such that a large source size can be partially compensated for by a smaller amount of limb-darkening, and vice versa. This may restrict our ability to predict the light curve shape while the source is inside the caustic region, though, as we show in §4.3, this restriction is not severe.

The model light curve produced by our best model is shown in Figure 1 with the PLANET data superposed. As the expanded views on the caustic regions show, this rotating binary fit is excellent; the solution reproduces our data in every detail. Binary lens rotation in MACHO 97-BLG-41 is not only detected, but rather well determined by the PLANET data: $\delta d = -0.070 \pm 0.009$ and $\delta\theta = 5°.61 \pm 0°.36$ represents $\sim 13\%$ and $\sim 6\%$ precision (1σ) for the magnitude of the radial and azimuthal motions on the sky, respectively. We find no other rotating solutions with similar χ^2, and suspect that none exists since the covariance matrix for the empirical parameters varies smoothly over a very wide range in χ^2 during our search.

The residuals of the ISIS cleaned data set from our best model are shown in Figure 4. Since we have assumed rectilinear motion of the lens components, systematic residuals with time measured from $t = (t_{cc,2} + t_{cc,1})/2$ might indicate accelerated motion. The absence of systematic effects of any kind in the residuals indicates that our assumption of rectilinear motion is a good approximation, but also implies that our data for MACHO 97-BLG-41 are not sufficient to detect the angular acceleration of the rotating binary components.

Our best fits indicate that the unblended color and magnitude of the source are $(V - I)_S = 2.51 \pm 0.03$ and $I_S = 16.82 \pm 0.02$, respectively. These uncertainties are independent because the first depends only on the ratio of V and I flux, while the latter depends on other model parameters. The blended light, whether from unrelated stars along the line of sight or from the lens itself, is quite faint: our best model yields blend magnitudes of $V_B = 22.8$, with errors large enough to make the detection unreliable, and $I_B = 20.09 \pm 0.47$. The small amount of blended light places a constraint on the mass of a stellar lens: a primary more massive than $M_1 = 1.4\,M_\odot$ (and hence a binary more massive than $M = 1.9\,M_\odot$) at any position between us and the Galactic bulge would produce a brighter blend than is observed. A spectrum taken by Lennon et al. (1997) during the second crossing may be able to exclude smaller binary masses if the blue (< 4500Å) unpublished portion of the spectrum fails to indicate the flux expected from less massive (hotter) stars.

Lennon et al. (1997) deduce from their high signal-to-noise spectrum that the source star is a cool giant with log $g = 3.2 \pm 0.3$, $T_{\mathrm{eff}} = 5000 \pm 200$, and [Fe/H]$= -0.2 \pm 0.2$ dex. Interpolating between the model limb-darkening grids of Claret, Díaz-Cordovés, and Giménez (1995), we estimate that such a source star would be expected to have a linear limb-darkening coefficient of $c_I = 0.56$. Limb darkening of the source, which affects the SAAO 1m data in the sharp decline after the second caustic crossing at HJD$' = 654.5$ and (to a lesser extent) the LaSilla data after the first crossing at HJD$' = 618.8$, can be measured from our light curve data alone. We find $\Gamma_I = 0.42 \pm 0.09$, corresponding to a linear limb-darkening coefficient of $c_I = 0.52 \pm 0.10$, in agreement with atmospheric models for a source of the type deduced by Lennon et al. (1997). Our V data do not meaningfully constrain Γ_V. The dereddened source color of $(V - I)_{S,0} = 1.07 \pm 0.05$ we derive in §5 together with isochrones of Bertelli et al. (1994) suggests $T_{\mathrm{eff}} = 4750 \pm 150$, somewhat cooler but consistent with that of Lennon et al. (1997).

4.3. Comparison with MACHO/GMAN Data

Our rotating binary solution makes use of only PLANET data, which unfortunately sample only two neighboring points near the first caustic and five points at the very end of the second caustic. Nevertheless, since our solution predicts the full light curve over these caustic intervals, we compare our prediction with the MACHO/GMAN data for this event, kindly provided to us by A. Becker (1999, private communication). These data were presented in Alcock et al. (1999) and incorporated into the analysis of Bennett et al. (1999), although with two different treatments of the systematic uncertainties.

We show the comparison between the PLANET model and MACHO/GMAN data for the full light curve of the event and for zooms of the first and second caustics in Figure 5. In order to determine the magnifications from the flux levels provided to us, we fit the fluxes to a function $F(t) = A(t)F_{S} + F_{B}$ where F_{B} is constrained to be non-negative and $A(t)$ is the magnification in our model at the time of observation t. The parameters F_{S} and F_{B} are the minimum required to convert from observed flux to magnification. No other fitting parameter was altered to accommodate the MACHO/GMAN data. The light curve is calculated using the I band limb-darkening coefficient $\Gamma_I = 0.42$. Although the MACHO/GMAN data were taken in other bands, this affects only a few points and those by only a small amount. The residuals of the MACHO/GMAN data from our model are shown in Figure 6.

Without accounting for possible systematics in the data through error bar rescaling, we find that our model produces a $\chi^2 = 2787$ for 1557 MACHO/GMAN data points. The same model produces a $\chi^2 = 2369$ for the 1317 MACHO/GMAN data points before or after the microlensing event, indicating that the large χ^2 is likely due to underestimated error bars and not due to problems in the model.

Overall, our model prediction derived from PLANET data is in good agreement with the MACHO/GMAN points, even though their data did not enter the fitting process in any way, including in the choice of initial model parameters. Even portions of the MACHO/GMAN light curve that are devoid of PLANET data are generally well matched by the PLANET model. The one exception is the *slope* of the two Wise 1m points at $\mathrm{HJD}' = 654.26$, which are separated by 0.004 days. While the model reproduces the midpoint of these two points almost exactly, it predicts a change of -0.5%, whereas the measured flux changes by $2.7 \pm 0.4\%$, a formal discrepancy of $8\,\sigma$, which is discernible but not obvious in Figure 5 due to horizontal compression. This conflict cannot be resolved by minor adjustments to the model: matching the data would require putting these two points in a very different place relative to the caustic structure, which cannot be accomplished without significant changes in the model parameters away from the global minimum found

using the PLANET data. Hence, if the PLANET model is even approximately correct, the errors on these two Wise points must be severely underestimated.

The MACHO error bars that we have used and shown in Figures 5 and 6 are those reported by the SoDoPhot photometry program with an additional 1.4% added in quadrature; this is the standard procedure used by the MACHO team to account for systematic uncertainties. The uncertainties displayed for the GMAN data from CTIO and Wise observatories are those reported from the ALLFRAME photometric package used for their reduction, and have not been modified in any way. As we discuss in §2, when fitting models to data with mis-estimated errors, rescaling must be done in order to weight one data set properly against another to obtain valid statistical error estimates for the derived parameters. A. Becker (1999, private communication) reports that in the MACHO/GMAN analysis (Alcock et al. 1999) the GMAN error bars were multiplied by a factor of 1.5, while D. Bennett (1999, private communication) reports that the MPS analysis (Bennett et al. 1999) added 1% in quadrature to the uncertainties for GMAN data sets. Since we do not have access to the raw data or even to their global characteristics (seeing, background, exposure time), we cannot offer an independent judgment. However, because we are not fitting models to these data, but only reporting their residuals from our model fit to PLANET data, there is no compelling reason to rescale. For completeness, we note that the residuals have $\chi^2 = 2787$ for 1557 data points with MACHO rescaling only (shown), and $\chi^2 = 2645$ and $\chi^2 = 2622$ under the two GMAN rescaling schemes listed above. Since 1489 of the total 1557 points are from the MACHO team, the difference in GMAN data rescaling has a small effect on the total χ^2.

One might ask how the PLANET model is able to fit MACHO/GMAN data in regions interior to the caustic where we have no data and where knowledge of the source size (relative to the Einstein ring) is crucial. The excellent PLANET coverage over the larger anomaly allows determination of q, d_{mid}, and the trajectory over the second caustic quite accurately, so the path of the center of the source through the caustic region is well known. Our data at the end of the second caustic crossing fix the time at which the limb of the source exits the caustic. Together, the timed trajectories of the source center and its limb allow us to determine the source size with a precision sufficient to match MACHO/GMAN caustic data.

5.   Physical and Kinematical Parameters of the Lens System

The proper motion is given by $\mu = \theta_*/t_*$ where θ_* is the angular radius of the source and t_* is the time required for the source to travel its own radius. Since the source trajectory

and total time for the source to cross the caustic are well-determined by our data, t_* is known accurately from our model. We find $t_* = \Delta t_2 \sin \phi = (0.193 \pm 0.005)$ days, where Δt_2 is the time for the egressing source radius to cross the second caustic and $\phi = 88.2°$ is the angle between the source trajectory and the caustic at this point.

From our best-fitting solution, we also find the unblended color and magnitude of the source, $(V - I)_S = 2.51$ and $I_S = 16.82$, which imply intrinsic colors of $(V - I)_{S,0} = 1.07$ and $I_{S,0} = 14.67$ using the extinction $A_I = 2.15$ and reddening $E(V - I) = 1.44$ we derived in §2.1 for this field. In order to determine the angular radius of the source, we rederive the empirical surface brightness-color relation of van Belle (1999), using the same data set but restricted to the domain $2.0 \leq V - K \leq 3.5$. These data were generously provided to us by G. van Belle (1999, private communication) in advance of publication. We obtain

$$\log(2\theta_*) + V/5 = 1.2885 \pm 0.0063 + (0.2226 \pm 0.0133)[(V - K)_0 - 2.823] \,, \qquad (4)$$

where the uncertainties are expressed so that they are uncorrelated, and the half-interval of the uncertainty corresponds to $\Delta\chi^2 = 1$. Note that throughout we have used θ_* to denote angular radius (typical of the microlensing field) not angular diameter (conventional in the field of angular-size determinations). We convert our derived color of the source $(V - I)_{S,0} = 1.07 \pm 0.05$, to $(V - K)_{S,0} = 2.40 \pm 0.15$ using the calibrations of Bertelli et al. (1994) (ATLAS9 models) and Bessel et al. (1998) (ATLAS9 + NMARCS models). These calibrations are nearly independent of metallicity and surface gravity. The surface brightness-color relation then yields an angular radius of the source of

$$\theta_* = (5.56 \pm 0.54) \, \mu\text{as} \,. \qquad (5)$$

The error in equation (5) assumes an intrinsic scatter of 8.7% in the van Belle (1999) surface brightness-color relation, which we judge from the excess in the scatter over measurement uncertainties, and includes the 2.0% standard error about the mean of the restricted relationship we have used as well as our measurement uncertainties in I, $(V - I)$, and A_I of 0.02, 0.03 and 0.08 mag, respectively. Even rather large ($\sim$0.5 mag), unrecognized errors in the extinction would have a small effect ($< 3.5\%$) on our estimate of θ_* because extinction is accompanied by reddening which affects the angular size estimate in the opposite sense.

We stress that the angular size can be determined much more accurately than the physical size (or distance) of the source. We have checked our determination based on van Belle's (1999) empirical relation with angular sizes predicted from the isochrones of Bertelli et al. (1994). We find that for a range of metallicities ($-0.4 \leq$[Fe/H]≤ 0) and ages (8 Gyr $\leq T \leq 12$ Gyr) that reproduce the intrinsic color $(V - I)_{S,0} = 1.07$ of the source, stellar radii and distances (inferred from our $I_{S,0} = 14.67$) vary by almost a factor of two. Despite this, the angular radii formed by the ratio of physical radius and distance are extremely

stable, within 2% of our slightly modified van Belle (1999) relation. We conclude that equation (5) is robust. Our estimate of θ_* is considerably larger than the $(2.9 \pm 0.7)\mu$as of Bennett et al. (1999); the cause of this is not completely clear.

Combining our measurements for θ_* and t_* yields

$$\mu = \frac{\theta_*}{t_*} = (50 \pm 5)\,\mathrm{km\,s^{-1}\,kpc^{-1}}, \tag{6}$$

which corresponds to $(400 \pm 40)\,\mathrm{km\,s^{-1}}$ projected onto the Galactic center at 8 kpc. This is somewhat higher than would be expected for a bulge source lensed by either a bulge or disk lens, although it could be consistent with either. This large proper motion is what one would expect for a disk lens lensing a disk source on the far side of the bulge. Since the source is close to the Galactic plane $(l, b) = (1.32, -1.94)$, such a geometry is not implausible.

5.1. Mass-Distance Relation

The Einstein ring radius can be estimated from our model and the proper motion estimate above as
$$\theta_{\mathrm{E}} = \mu\, t_{\mathrm{E}} = (700 \pm 70)\,\mu\mathrm{as}. \tag{7}$$
Hence, from equation (1), we obtain the mass-source distance relation

$$\left(\frac{M}{M_\odot}\right)\left(\frac{1-x}{x}\right)\left(\frac{D_{\mathrm{S}}}{8\,\mathrm{kpc}}\right)^{-1} = 0.47 \pm 0.10, \qquad \text{where } x \equiv \frac{D_{\mathrm{L}}}{D_{\mathrm{S}}}. \tag{8}$$

If the lens were luminous and in the bulge, the total mass would be constrained by the mass of the turnoff to be $M = (1+q)M_1 \lesssim 1.5\,M_\odot$. Hence, equation (8) implies $x \lesssim 0.75$. Since lens-source separations are distributed $\sim [1 + (1-x)^2/4(l^2 + b^2)]^{-1}$ where $2(l^2 + b^2)^{1/2} \sim 0.08$ (Gould 2000), this tends to argue against the lens being in the bulge. We make this argument more quantitative in the next section.

5.2. Statistical Estimate of Binary Lens Mass, Distance and Rotational Period

From the measurements of d_{mid}, δd, $\delta\theta$, and θ_{E}, we can determine the projected separation r_p and the projected relative velocity $\vec{v}_p$ of the binary up to a scale set by the lens distance D_{L}. We use coordinates parallel and transverse to the separation vector d_{mid} and consider only leading-order terms in δd and $\delta\theta$. One then obtains $r_p = d_{mid}\,\theta_E D_{\mathrm{L}}$ and

$\vec{v}_p = (\delta d/\delta t,\, d_{mid}\,\delta\theta/\delta t)\,\theta_E D_{\rm L}$. Inserting the parameter values determined from our model, we then find

$$r_p = 1.4\,{\rm AU}\left(\frac{D_{\rm L}}{4\,{\rm kpc}}\right), \qquad \vec{v}_p = (-9.7, 6.9)\,{\rm km\,s^{-1}}\left(\frac{D_{\rm L}}{4\,{\rm kpc}}\right). \tag{9}$$

These measurements can be combined with Kepler's Third Law to estimate the mass and distance of the lens. To do so, we assume that binaries of the observed mass ratio $q = 0.34$ are distributed along the line of sight in proportion to the density of their primaries, that they have a period distribution as measured by Duquennoy & Mayor (1991) for G stars in the solar neighborhood, that they are randomly oriented, and that they are uniformly distributed in e^2, where e is the eccentricity. We assume that the disk population has an exponential scale length of 3 kpc, an exponential scale height that varies linearly from 300 pc in the solar neighborhood to 100 pc near the Galactic center, and a local surface density in stars and brown dwarfs of $35\,M_\odot\,{\rm pc}^{-2}$. We further assume that the bulge can be approximated as an isothermal sphere with a rotation speed of $220\,{\rm km\,s^{-1}}$, truncated at 4 kpc from its center. We take the mass function to be $dN/dM \propto M^{-1}$ for both the disk and bulge, but with a cutoff of $M_1 \leq 1.1\,M_\odot$ for the bulge.

We perform a Monte Carlo integration in order to find the relative probability densities of the mass, distance, and period of the binary. First, we construct a set of random realizations of the orientation, eccentricity, and eccentric anomaly ψ (Goldstein 1980) of the binary. For each realization, we determine three quantities: $w_r \equiv r_p/a$, $w_v^2 \equiv v_p^2/\langle v^2\rangle$, and $\cos\Phi \equiv \mathbf{r}_p \cdot \mathbf{v}_p/(r_p v_p)$, where a is the semi-major axis of the binary and $\langle v^2\rangle$ is its time-averaged square velocity. We first ask whether $\cos\Phi$ is near (i.e., within 10%) of the observed value of $\delta d/[(\delta d)^2 + (d_{\rm mid}\,\delta\theta)^2]^{1/2} = -0.81$. If it is not, we skip to the next realization. If it is, we use Kepler's Law and the Virial Theorem, $GM = a\langle v^2\rangle$, to find the period consistent with the observed parameters

$$P = 2\pi\,\frac{w_v}{w_r}\,\frac{d_{\rm mid}\,\delta t}{[(\delta d)^2 + (d_{\rm mid}\,\delta\theta)^2]^{1/2}} = 3.59\frac{w_v}{w_r}\,{\rm yr}. \tag{10}$$

Next, by eliminating M in the Virial Theorem in favor of θ_E, the value of which is fixed by equation (7), we obtain

$$x^2(1-x) = w_r w_v^2\left(\frac{c\delta t}{2D_{\rm S}}\right)^2\left(\theta_{\rm E}\,d_{\rm mid}\,[(\delta d)^2 + (d_{\rm mid}\,\delta\theta)^2]\right)^{-1} = 0.265\,w_r w_v^2, \tag{11}$$

where we have assumed $D_{\rm S} = 8\,{\rm kpc}$ in the evaluation. If $w_r w_v^2 > 0.559$, this equation has no solution and we skip to the next realization. Otherwise, we find the two solutions and the corresponding masses from equation (8). If the higher-mass solution has $M > 1.9\,M_\odot$

we eliminate it because the lens would have then given rise to detectable blended light (which is not observed: see §4.2 and Table 1). For bulge lenses we eliminate stars above the turnoff, $M > 1.5 M_\odot$ (i.e., $M_1 > 1.1 M_\odot$). Finally, we weight each realization by the following factors: 1) $dt/d\psi = 1 - e \cos \psi$ to take account of the amount of time spent at each phase ψ, 2) the density of lenses at x, 3) two factors of x, one for the cross section for lensing ($\propto x\theta_E$) and one for the transverse flux of lenses relative to the sources ($\propto x\mu$), 4) factors to account for the mass function and period distribution as described above, and 5) factors to account for the transformation from the theoretical quantities (x, M, P) to the observables $(d_{\mathrm{mid}}, \delta d, \delta \theta)$. The most important of these last factors is that for x, which scales $\propto |x(1 - x)/(2 - 3x)|$, diverging at $x \sim 2/3$ thus compensating for the small number of simulated events near this value. Note that the factors in (3) are actually $\propto D_L \theta_E$, but since θ_E is measured and $D_S \sim 8$ kpc is approximately known, they can be taken as $\propto x$.

Figure 7 shows the results of this Monte Carlo integration for the lens distance, mass and orbital period, respectively. The noise near $x = 2/3$ and $M \sim 0.95 \, M_\odot$ is due to the low sampling rate and corresponding large transformation factor described above. The probability is five times greater that the lens is in the disk than in the bulge. Note that the peaks of the probability distributions for the lens mass and distance do not correspond to the same solution. If the lens is in the disk, the probability distribution for its total mass peaks at that of an M-dwarf binary with $M \sim 0.3 \, M_\odot$, corresponding (from eq. 8) to a lens distance of $D_L \sim 3.1$ kpc for a source distance of $D_S \sim 8$ kpc. The peak at $D_L \sim 5.5$ kpc of the probability distribution for the lens distance, on the other hand, corresponds to a total mass $M \sim 1.03 \, M_\odot$. The probability distribution for the orbital period is rather sharply peaked around 1.5 yr. A firm detection of acceleration in the relative motion of the lens components would tighten the constraints on mass, distance and orbital period beyond that made possible by our detection of their relative velocity.

In order for an orbit to be bound, the ratio $r v^2/2 GM$ must be less than unity. Solutions derived from our Monte Carlo procedure are bound by construction. It can be shown that for any such solution, equation (11), together with the Virial Theorem and the definitions of w_r and w_v, yields a constraint on this ratio for face-on orbits, namely

$$\frac{r_p v_p^2}{2 \, GM} = \frac{x^2 \, (1 - x)}{0.53} \quad . \tag{12}$$

Since the right-hand side has an upper bound of 0.28 at $x = 2/3$, all such orbits are quite comfortably bound for any value of x. Only orbital phases and inclinations that would increase this ratio by a factor of four would result in unbound orbits.

6. Conclusions

We have presented our photometric data set for the complex MACHO 97-BLG-41 event, consisting of 325 points in the I and 46 points in the V photometric passbands taken during the four month period in which the event was in progress. The light curve displays two anomalous regions that cannot be fit by a static binary lens, in agreement with a similar conclusion by Bennett et al. (1999) modeling an independent data set. Unlike Bennett et al. (1999), however, we find that a rotating binary provides an excellent fit to our data. We measure changes in the binary separation (in units of the Einstein ring radius) of $\delta d = -0.070 \pm 0.009$ and in the binary orientation on the sky of $\delta\theta = 5°.61 \pm 0°.36$ during the 35.17 days between the separate caustic events, the first clear observational evidence for rotation in a binary microlens.

Our success in finding this rotating solution was facilitated by the high quality of our data for this event and by three strategic choices: (1) searching for a solution involving only the first-order rectilinear component of the relative motion of the binary on the sky, (2) fitting an empirical parameter set that is best constrained by the light curve rather than the equivalent, but more non-linear canonical parameter set, and (3) searching on a grid of solutions until a gross minimum is found rather than relying on downhill simplex methods only to search for approximate minima.

Bennett et al. (1999) used the MACHO/GMAN data set to reach their conclusion that a three-lens system (binary + Jovian planet) was indicated in MACHO 97-BLG-41. In contrast, we find that our rotating binary model provides a good fit to the same data with fewer additional degrees of freedom, even though the MACHO/GMAN data were not used in any way to fix the physical binary parameters and include points in caustic regions that our data do not sample well. Furthermore, the particular three-body model presented by Bennett et al. (1999) is strongly inconsistent with our data near the first anomaly in the light curve of MACHO 97-BLG-41. We conclude that a third body is not required, and that binary lens rotation provides a natural, physically-motivated and physically plausible explanation of the light curve of MACHO 97-BLG-41.

Our modeling also produces a limb-darkening parameter for the background K giant corresponding to $c_I = 0.52 \pm 0.10$, in agreement with models of stellar atmospheres for this type of star. Combining our physical and kinematic measurements with reasonable assumptions for the distributions in space and separation of Galactic binaries, we are able for the first time to derive kinematic probability distributions for the total mass and period of a binary microlens; for MACHO 97-BLG-41, these peak at $0.3\,\mathrm{M_\odot}$ and 1.5 yr, respectively.

Acknowledgments

REFERENCES

Afonso, C., et al. (EROS Collaboration) 1998, A&A, 337, L17

Afonso, C., et al. (EROS, MACHO, MPS, OGLE, & PLANET Collaborations) 2000, ApJ, 532, in press (astro-ph/9907247)

Alard, C. 1999, A&A, submitted (astro-ph/9903111)

Albrow, M. D., et al. (PLANET Collaboration) 1998, ApJ, 509, 687

Albrow, M. D., et al. (PLANET Collaboration) 1999a, ApJ, 522, 1011

Albrow, M. D., et al. (PLANET Collaboration) 1999b, ApJ, 522, 1022

Albrow, M. D., et al. (PLANET Collaboration) 1999c, ApJ, submitted (astro-ph/9909325)

Alcock, C., et al. (MACHO Collaboration) 1997, ApJ, 479, 119

Alcock, C., et al. (MACHO/GMAN Collaboration) 1999, ApJ, submitted (astro-ph/9907369)

Bennett, D. P., et al. 1999, Nature, 402, 57

Bertelli, G., Bressan, A., Chiosi, C., Fagotto, F., & Nasi, E. 1994, A&AS, 106, 275

Bessell, M. S., Castelli, F., & Plez, B. 1998, A&A, 333, 231

Butler, R. P., Marcy, G., Williams, E., Hauser, H., & Shirts, P. 1997, ApJ, 474, L115

Claret, A., Díaz-Cordovés, J., & Giménez, A. 1995, A&AS, 114, 247

Cochran, W., Hatzes, A., Butler, P., & Marcy, G. 1997, ApJ, 483, 457

Dominik, M. 1998, A&A, 329, 361

Dominik, M. 1999, A&A, 349, 108

Duquennoy, A., & Mayor, M. 1991, A&A, 248, 485

Erdl, H., & Schneider, P. 1993, A&A, 268, 453

Gaudi, B. S., & Sackett, P. D. 2000, ApJ, 529, in press (astro-ph/9904339)

Goldstein, H. 1980, Classical Mechanics (Reading MA: Addison-Wesley)

Gould, A. 2000, ApJ, submitted (astro-ph/9906472)

Kiraga, M., & Paczyński, B. 1994, ApJ, 430, 101

Lennon, D. J., Mao, S., Reetz, J., Gehren, T., Yan, L., & Renzini, A. 1997, ESO Messenger, 90, 30 (astro-ph/9711147)

Mao, S., & Paczyński, B. 1991, 374, L37

Menzies, J. W., Cousins, A. W. J., Banfield, R. M., & Laing, J. D. 1989, SAAO Circulars, 13, 1

Paczyński, B., Udalski, A., Szymański, M., Kubiak, M., Pietrzyński, G., Soszyński, I., Woźniak, P., & Żebruń, K., 1999, Acta Astron., 49, 319 (astro-ph/9908043)

Rhie, S. H., Becker, A. C., Bennett, D. P., Fragile, P. C., Johnson, B. R., King, L. J., Peterson, B. A., & Quinn, J. (MPS Collaboration) 1999a, ApJ, 522, 1037

Rhie, S. H., et al. (The MPS and MOA Collaborations) 1999b, ApJ, 532, 000 (astro-ph/9905151)

Schechter, P. L., Mateo, M., & Saha, A. 1993, PASP, 105, 1342

Schneider, P., & Weiss A., 1986, A&A, 164, 237

Stanek, K. Z. 1996, ApJ, 460, L37

Thorsett, S. E., Arzoumanian, Z., Camilo, F., & Lyne, A. G. 1999, ApJ, 523, 763

Udalski, A., Szymański, M., Mao, S., Di Stefano, R., Kałużny, J., Kubiak, M., Mateo, M., & Krzemiński, W. 1994, ApJ, 436, L103

van Belle, G. T. 1999, PASP, in press (astro-ph/9904295)

Witt, H. J., & Mao, S. 1995, ApJ, 447, L105

Zhao, H. S., Spergel, D. N., & Rich, R. M. 1995, ApJ, 440, L13

Table 1.   Photometric Parameters fitted to Cleaned PLANET Data for
MACHO 97-BLG-41

Data Set	# Points	$\sigma/\sigma_{\mathrm{ISIS}}$	η'_{see}[a]	I_S[b]	I_B[b]
I BAND					
SAAO 1m	97	1.15	-0.0270	16.82	20.12
ESO/Dutch 0.9m	58	1.59	-0.0178	16.82	20.33
Canopus 1m	95	0.73	-0.0632	16.81	19.44
CTIO 0.9m	49	1.55	-0.0290	16.89	21.57
Perth 0.6m	26	1.21	-0.0141	16.81	19.00
V BAND					
SAAO 1m	14	1.45	0.2725	19.33	22.84
ESO/Dutch 0.9m	18	0.92	-0.1304	19.38	22.03
Canopus 1m	14	0.34	-0.1508	19.43	19.56

[a]The parameter η'_{see} is related to the seeing correlation parameter η_{see} of §3 by $\eta'_{\mathrm{see}} = \eta_{\mathrm{see}}/(F_{\mathrm{S}} + F_{\mathrm{B}})$, and thus has units of arcsec^{-1}.

[b]Fluxes F_{S} and F_{B} have been converted to standard Johnson V and Cousins I magnitudes.

Table 2.   Geometric Parameters fitted to Cleaned PLANET Data
for MACHO 97-BLG-41

	Empirical		Canonical[a]
d_{mid}	0.5122 (0.0015)	d_0	0.4787
q	0.3434 (0.0065)	q	0.3434
$t_{cc,1}$	619.18 (0.03) days	t_E	24.175 days
$t_{ce,2}$	654.544 (0.001) days	t_0	653.4254 days
$u_{c,1}$	0.0020 (0.0005)	u_0	0.07229
ℓ_2	0.028 (0.001)	α	112.37
Δt_2	0.193 (0.005) days	ρ_*	0.00796
δd	-0.070 (0.009)	Δ_x	-0.0467
$\delta\theta$	$5°.61$ ($0°.36$)	Δ_y	0.0366
Γ_I	0.42^{b}(0.09)	c_I	0.455^{b}

[a]Precision given in canonical parameters is necessary to reproduce the model, but the last two digits are generally uncertain.

[b]For the empirical parameters, Γ_I corresponds to $c_I = 0.52\pm0.10$; for the canonical parameters, c_I corresponds to $\Gamma_I = 0.358$. For a discussion, see §4.2.2.
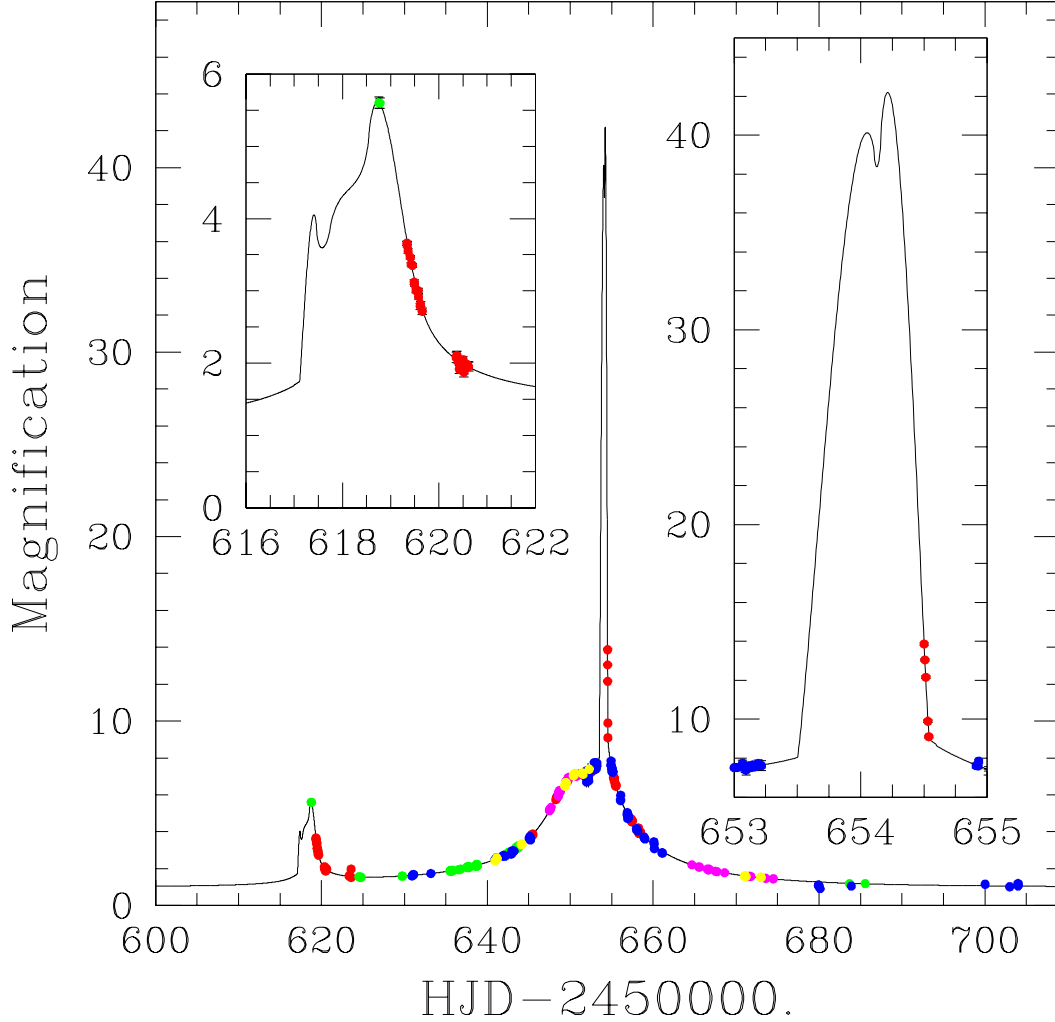
Fig. 1.— Our best rotating binary model shown with cleaned PLANET multi-site data in the *V* and *I* passbands (*Green:* Dutch/ESO 0.91m, LaSilla, Chile; *Red:* SAAO 1m, Sutherland, South Africa; *Blue:* Canopus 1m, Tasmania, Australia; *Yellow:* CTIO 0.9m, Cerro Tololo, Chile; *Magenta:* Perth 0.6m, Bickley, Western Australia). Rescaled error bars (§4.2.2) are shown, but are generally smaller than the size of the points. Insets are zooms on the two caustic crossing regions. Plotted is magnification versus HJD′.
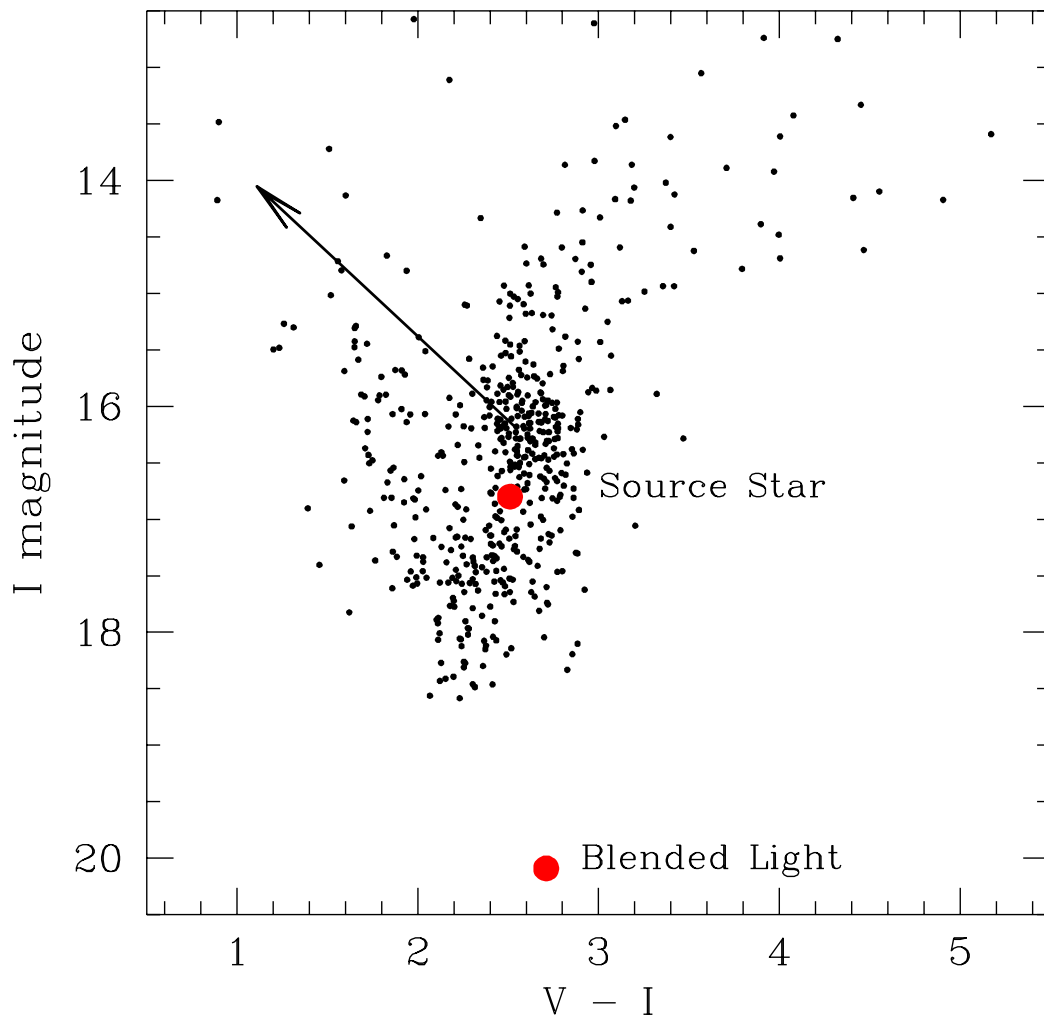
Fig. 2.— Calibrated color-magnitude diagram taken from SAAO 1m observations of a $1' \times 1'$ field centered on MACHO 97-BLG-41. The position of the unmagnified source and much fainter blend (as determined from our modeling) are indicated by the large solid dots. The dereddening vector connecting the center of the observed red clump to the intrinsic clump characterized by Paczyński et al. (1999) is also shown.
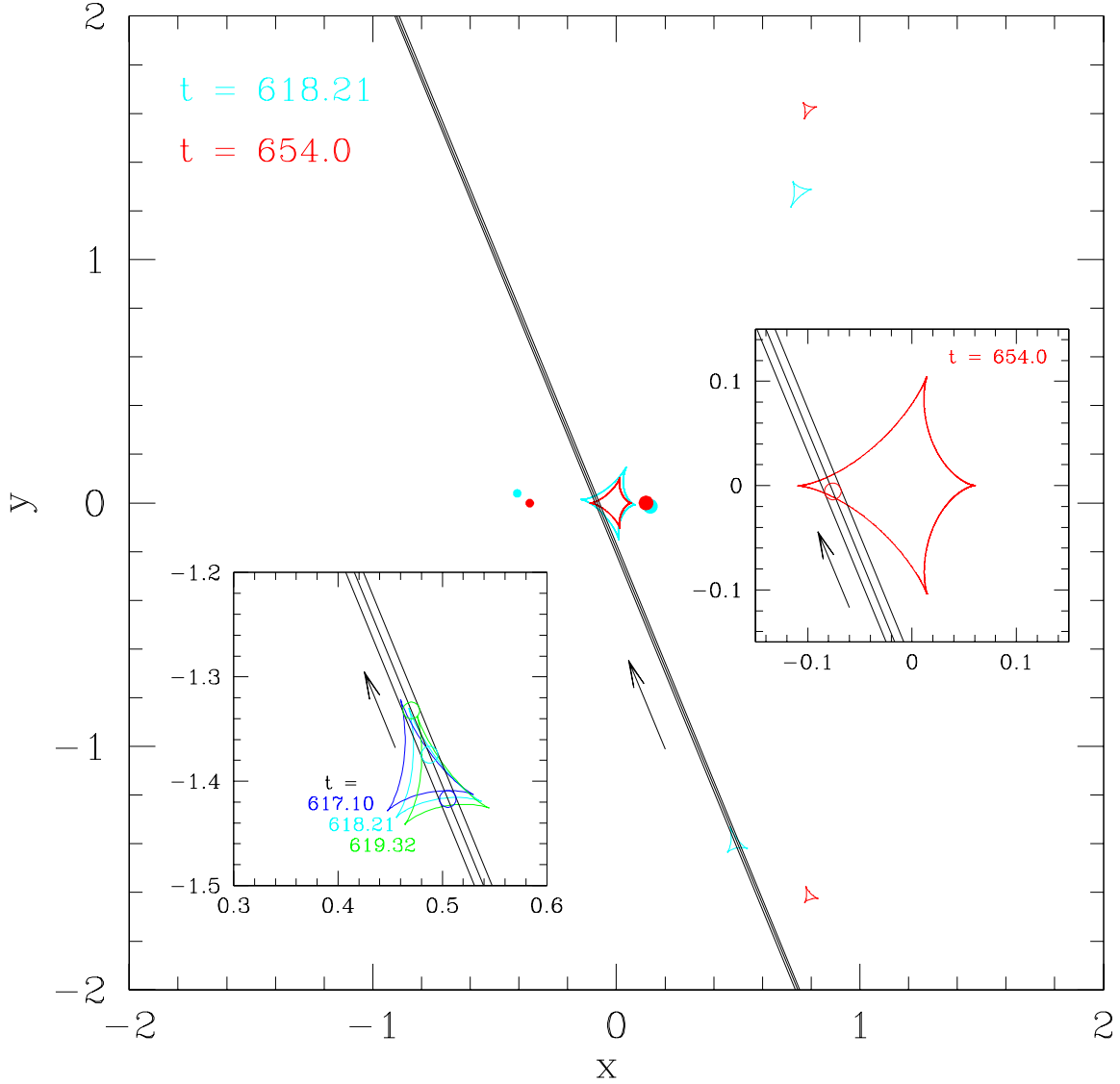
Fig. 3.— The caustic topology of our best-fitting rotating model is shown at times near the first and second caustic crossings. Units are angular Einstein radii $\theta_{\rm E}$. The straight line shows the source trajectory and the arrow its direction of motion. The binary components are shown as small dots. As time progresses, the binary rotates counterclockwise (causing the caustic pattern to do the same) and the component lenses move closer together (increasing the separation between the triangular outer caustics and the central caustic). The zooms better illustrate the source (circle) trajectory as it crosses the central caustic (right) and triangular caustic (left). The triangular caustic movement during the entire first crossing is shown. The source diameter is indicated by the distance between the parallel lines.
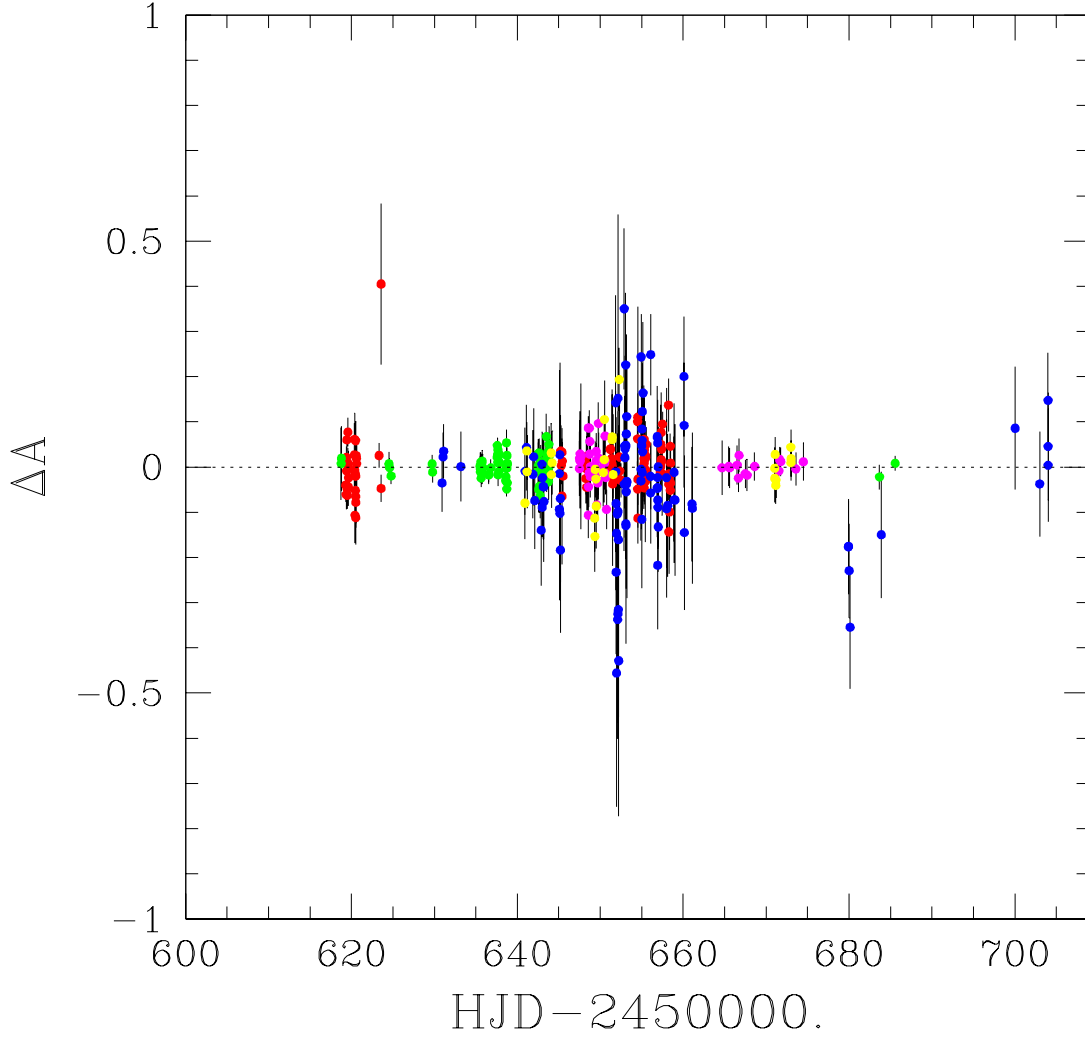
Fig. 4.— Magnification residuals (data − model) of the cleaned PLANET data set from our best-fitting rotating binary model are shown as a function of HJD′. The color coding follows that of Fig. 1. Error bars have been rescaled to account for systematics (§4.2.2). Full moon occurred at HJD′ = 620 and HJD′ = 649.
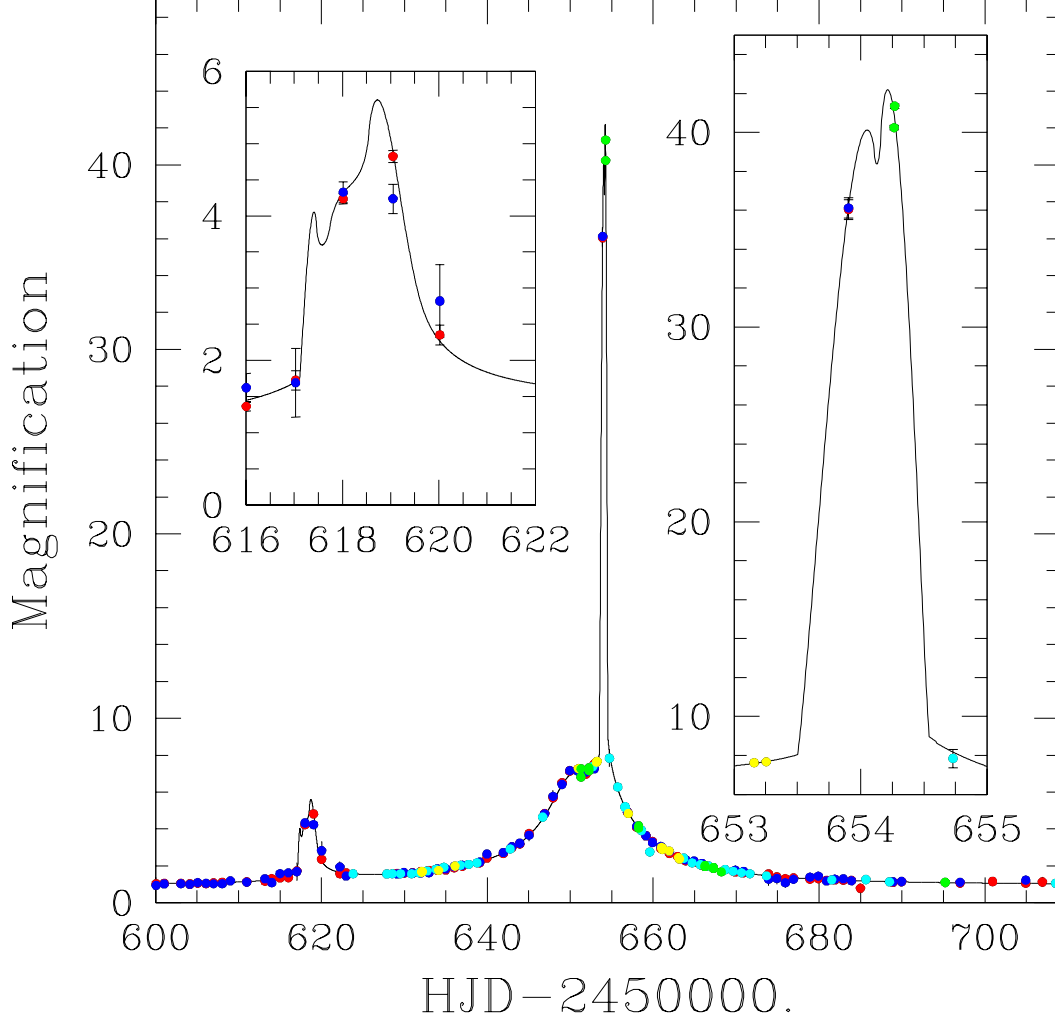
Fig. 5.— The curves show the magnification of MACHO 97-BLG-41 as a function of time derived from the best-fitting model to the PLANET data, and are thus identical to those in Fig. 1. The points are data from the MACHO/GMAN collaboration kindly provided by A. Becker (1999, private communication). These data points did not enter the fit in any way: they are simply superposed on the model curve after undergoing a linear transformation to convert from flux to magnification. Color coding indicates observing site and passband (*Red:* MACHO R; *Blue:* MACHO B; *Cyan:* CTIO 0.9m R; *Yellow:* MSO 0.8m R; *Green:* Wise 1m R). Insets show the same two zooms displayed in Fig. 1. The agreement in regions devoid of PLANET data, near the beginning of the first caustic crossing and throughout the bulk of the second crossing, is particularly striking.
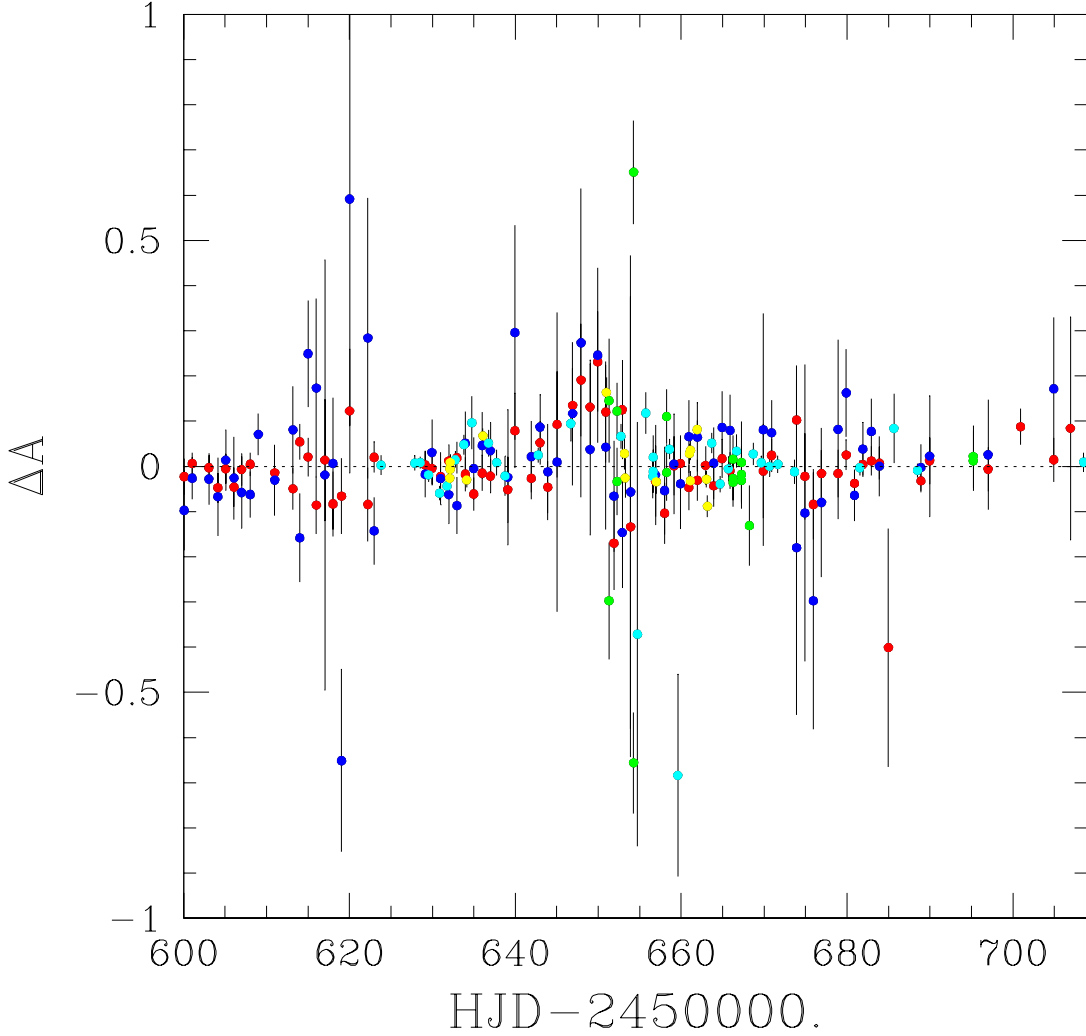
Fig. 6.— Magnification residuals of the MACHO/GMAN data from our best-fitting model to the PLANET data only are shown as a function of HJD'. The color coding follows that of Fig. 5. MACHO error bars have been multiplied by a customary 1.4 to account for systematics. Error bars for GMAN data are those reported by the crowded field reduction packages; no attempt has been made here to increase the size of the GMAN error bars to account for systematic uncertainties (§4.3). Full moon occurred at HJD' = 620 and HJD' = 649.
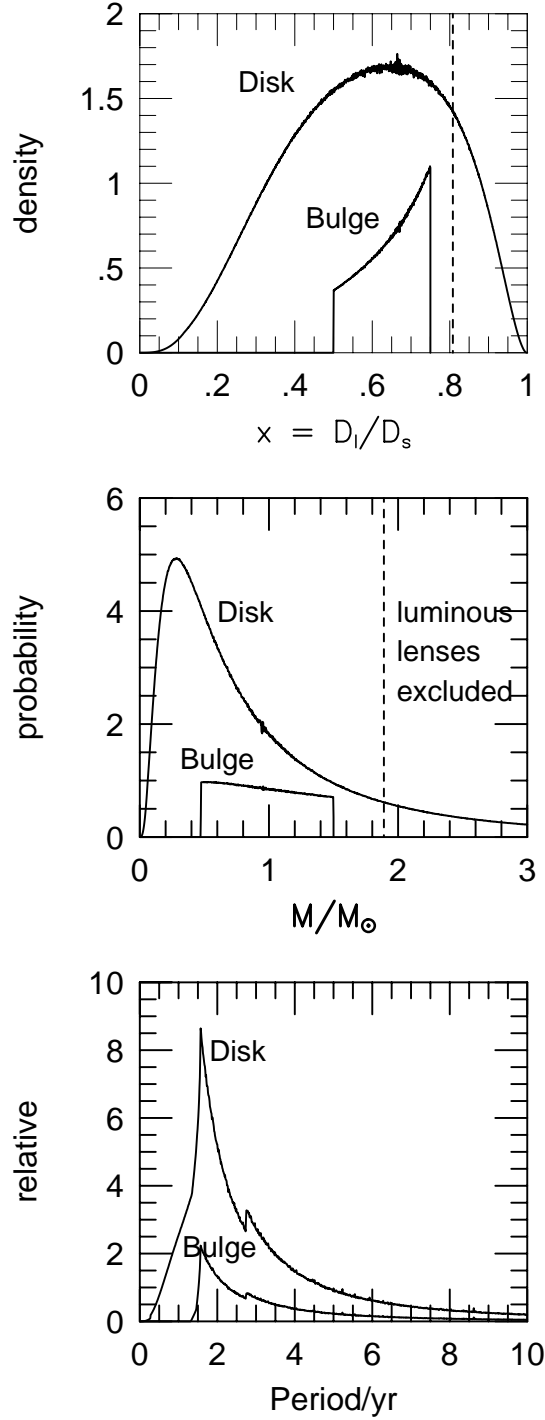
Fig. 7.— Physical properties of the binary derived from the rotation measurement and other observational constraints (see §5.2). *Top:* Relative probability density of lens distances $D_{\rm L}$ expressed as fraction x of the source distance $D_{\rm S}$. The upper and lower lines are for disk and bulge lenses, respectively. *Middle:* Same for the total mass of the binary lens. *Bottom:* Same for the orbital period of the binary. To the right of the dashed vertical lines luminous (stellar) lenses are excluded, since their mass would then correspond to more blended light than is observed. Bulge lenses have a lower distance cutoff (imposed by the simplistic bulge model) and an upper mass cutoff (imposed by the mass of bulge turnoff stars) which translate into mass and distance limits, respectively, through eq. (8).